Microchimica Acta (2020) 187:450
https://doi.org/10.1007/s00604-020-04434-0

ORIGINAL PAPER

Rolling circle amplification promoted magneto-controlled photoelectrochemical biosensor for organophosphorus pesticides based on dissolution of core-shell MnO_2 nanoflower@CdS mediated by butyrylcholinesterase

Juan Tang[1] · Jingjing Li[1] · Pengyuan Xiong[1] · Yuanfang Sun[1] · Zhiyao Zeng[1] · Xiaochun Tian[2] · Dianping Tang[3]

Received: 6 February 2020 / Accepted: 7 July 2020

Abstract

A photoelectrochemical (PEC) aptasensing platform is devised for sensitive detection of an organophosphorus pesticide based on dissolution of core-shell MnO_2 nanoflower@CdS (MnO_2 NF@CdS) by thiocholine (TCh). TCH is produced from the butyrylcholinesterase-acetylthiocholine system, accompanied by target-triggered rolling circle amplification (RCA). The core-shell MnO_2 NF@CdS with excellent PEC performance was synthesized and employed as a photo-sensing platform. The target was detected on a functionalized magnetic probe with the corresponding aptamer. Upon malathion introduction, the aptamer was detached from the magnetic beads, while capture DNA (cDNA, with primer fragment) remained on the beads. The primer fragment in cDNA can trigger the RCA reaction to form a long single-stranded DNA (ssDNA). Furthermore, a large number of butyrylcholinesterase (BChE) were assembled on the long ssDNA strands through the hybridization with the S_2-Au-BChE probe. Thereafter, TCh generated from hydrolysis of ATCh by BChE can reduce MnO_2 NF (core) to Mn^{2+} and release the CdS nanoparticles (shell) from the platform electrode, significantly enhancing the PEC signal. Under optimal conditions, the proposed aptasensor exhibited high sensitivity for malathion with a low detection limit of 0.68 pg mL^{-1}. Meanwhile, it also presents outstanding specificity, reproducibility, and stability. Importantly, the sensing platform provides a new concept for detection of pesticide.

Keywords Photoelectrochemical biosensor · Malathion · Core-shell MnO_2 NF@CdS nanostructure · Rolling circle amplification

Introduction

Organophosphorus pesticides (OPs; as a type of commonly used pesticide) have been widely used for insect control (both in residential and agricultural environments) owing to their insecticidal efficiency [1, 2]. However, OPs can cause a serious human and animal's health problem due to their neurotoxicity that can inhibit the activity of nervous system acetylcholine esterase even at low concentrations [3, 4]. Thus, there is an urgent demand for development of reliable methods for sensitive detection of organophosphorus pesticides. Recently, sustained endeavors have been made to construct reliable method, including mass spectrometry, high-performance liquid chromatography, and gas chromatography method [5–7]. Despite the considerable accuracy and precision in these methods, they suffer from sophisticated instrumentation, specialized staff, and associated high-costs, which inhibit their extensive applications. Hence, the design of simple and

Electronic supplementary material The online version of this article (https://doi.org/10.1007/s00604-020-04434-0) contains supplementary material, which is available to authorized users.

✉ Juan Tang
tjhere@126.com

[1] Ministry of Education Key Laboratory of Functional Small Organic Molecule, Department of Chemistry and chemical engineering, Jiangxi Normal University, Nanchang 330022, People's Republic of China

[2] Institute of Urban Environment, Chinese Academy of Sciences, Xiamen 361021, People's Republic of China

[3] Key Laboratory of Analysis and Detection for Food Safety (Ministry of Education of China and Fujian Province), Department of Chemistry, Fuzhou University, Fuzhou 350108, People's Republic of China

reliable method with good sensitivity and selectivity is more important and of interest.

Photoelectrochemical bioanalysis, a vibrantly developing analytical method, has gained substantial attention due to the interesting characteristics including high signal to noise ratio, low background, and excellent analytical performance [8–11]. Additionally, it operates with cheaper and simpler instrumentation. Accordingly, it has aroused considerable research interest in detection of multiple analytes, such as metal ions, glucose, cancer biomarker, thrombin, and microRNA [10–15]. In the past years, massive effort has been made on PEC bioassay exploitation and tremendous progress has been achieved. However, the detection mode of PEC bioassay platform is still limited, which makes it not adequately flexible to meet the various detection demands. Therefore, exploring new signal transduction mode with high sensitivity is highly desirable. Essentially, the PEC detection relies on the photoelectric transform efficiency of the photoactive substances. Thus, choosing the proper photoactive materials with high sensitive response is of vital importance to the performance of the PEC biosensor.

Cadmium sulfide (CdS), as an II-VI type semiconductor with a narrow direct band gap (~ 2.42 eV) and relatively negative conduction band, has shown prominent potential for application in photochemical catalysis, and solar cells [16, 17]. Nevertheless, the CdS nanoparticles (CdS NPs) with small size are easily aggregated together, which induce a higher recombination rate of photoexcitation electron-hole pairs that significantly affect its PEC performances [18, 19]. MnO_2 nanoflower (MnO_2 NF) has emerged as the most promising materials ascribed to its high specific surface area, inherently low toxicity, and low cost, which makes it an attractive candidate for support [20]. More importantly, recent reports have demonstrated that MnO_2 NF with the narrow band gap shows high capacity for visible light absorption [21, 22]. Thus, when MnO_2 NF coupled with CdS NPs, the well-matched energy levels of the two semiconductors can accelerate the transfer of the electron and hole, which can efficiently suppress the photo-corrosion of pure CdS NPs as well as enhance the photocurrent of MnO_2 NF [23]. Interestingly, MnO_2 nanomaterials with the intermediate valence exhibited strong oxidation ability and can be converted to Mn^{2+} by reducing substances, thus makes it a favorable candidate for photocurrent mediator [1, 24]. Generally, the reductive species comes from the enzymatic reaction in biosensing strategy [25]. Thus, the PEC performance of the bioassay can be improved via increasing the amount of enzyme, which assures high sensitivity.

Rolling circle amplification (RCA) is a powerful and simple isothermal amplified method mediated by polymerases, in which a long single-stranded DNA molecule containing large numbers of programmable tandem repeating sequences was synthesized [26, 27]. The RCA products that contain multiple repeats can be used as scaffolds for assembling with functional moieties (e.g., fluorophores, nanomaterials, and enzyme) modified complementary oligonucleotides, which makes it to be an efficiency tool for nanobiotechnology and biomedical research [28, 29]. Thus, taking advantages of the RCA-amplified method and MnO_2 NF–based photoactive substance, a simple but sensitive split-type PEC approach for detection of OPs was proposed. As designed, core-shell MnO_2 NF@ CdS heterostructure was synthesized and used for photoactive materials. Experiment results shows that it exhibited excellent photocurrent responses and stability under illuminations. Upon introduction of thiocholine (TCh), it will destroy the MnO_2 NF within MnO_2 NF@CdS nanostructure and cause the release of CdS NPs, thus obviously decrease the photocurrent signal. Meanwhile, the signal can be significantly enhanced by employed RCA-amplified technique. In the assay, the TCh was produced by butyrylcholinesterase (BChE) which modified on the RCA product through Au-modified complementary DNA. Relying on the high load of RCA products and excellent performance of the MnO_2 NF@CdS, the proposed sensor permits ultrasensitive PEC detection of target molecule.

Experimental

Materials and chemicals

Manganese sulfate monohydrate ($MnSO_4 \cdot H_2O$), potassium permanganate ($KMnO_4$), cadmium acetate dehydrate ($Cd(CH_3COO)_2 \cdot 2H_2O$), thiourea ($CH_4N_2S$), triethanolamine, and sodium citrate dehydrate ($Na_3C_6H_5O_7 \cdot 2H_2O$) were acquired from Aladdin (Shanghai, China). T4 DNA ligase, Phi29 DNA polymerase, and dNTP were purchased from New England Biolabs Ltd. Magnetic bead modified with streptavidin (Strep-MB) were purchased from Tianjin BaseLine Chrom Tech Research Centre. Chloroauric acid ($HAuCl_4 \cdot 3H_2O$), malathion, acetylthiocholine (ATCh), and butyrylcholinesterase (BChE) were supplied by Sigma-Aldrich. Sample of apple juice containing malathion was purchased from Kangtan Biotechnology Co. Ltd. (Guangdong, China). Ultrapure deionized water (18.2 MΩ cm) obtained from a Milli-Q water purification system.

All synthetic DNA used in this work was provided by Sangon Biotech Inc. (Shanghai, China). Their sequences were listed as follows:

Capture DNA (cDNA): 5′–biotin–TTT TTA TAC GGG AGC CAA CAC CAG CAG TCA AGA AGT TAA GAG AAA AAC AAT TGT GTA TAA GAG CAG GTG TGA CGG ATT GAG CAT AAT AGT TCC ACA GTT AC–3′.

Aptamer probe (Apt): 5′–ATC CGT CAC ACC TGC TCT TAT ACA CAA TTG TTT TTC TCT TAA CTT CTT GAC TGC TGG TGT TGG CTC CCG TAT–3′.
Padlock probe (pDNA): 5′–TAT TAT GCT CA**T CAG AAC TCA CCT GTT AG**G TAA CTG TGG AAC–3′.
Assist DNA-2 (S_2): 5′–NH_2–**GAT TGT CCA CTC AAG ACT**–3′.

Fabrication of core-shell MnO_2 NF@CdS nanocomposite

Firstly, the MnO_2 NF was synthesized by a hydrothermal method according to previous literature [30]. Generally, 1.0 g of $KMnO_4$ and 0.4 g of $MnSO_4{\cdot}H_2O$ were initially added into the 30 mL deionized water. Then, the mixture was heated in a 50 mL Teflon-lined stainless-steel autoclave at 140 °C for 30 min. After centrifuged and washed, the purified MnO_2 NFs were dried at 70 °C for 6 h in oven.

Next, the core-shell MnO_2 NF@CdS nanocomposite was synthesized in accordance with the literature with minor modification [31]. Briefly, 20 mL of the MnO_2 NF dispersion (2.5 mg mL^{-1}) was mixed with Cd $(CH_3COO)_2{\cdot}2H_2O$ (2.6 mM, 5 mL), CH_4N_2S (1.8 mM, 5 mL) and triethanolamine (50 wt%, 100 μL), and then kept stirring for 2 h. Thereafter, the above solution was heated in an autoclave at 140 °C for 36 h. Finally, the obtained core-shell MnO_2 NF@CdS nanocomposite was washed and dried at room temperature for 12 h.

Synthesis of the S_2-Au-BChE signal probe

The S_2-Au-BChE signal probe was prepared similarly to our previously work. Initially, gold nanoparticles were synthesized with a hydrothermal method [31]. Generally, 20 mL $Na_3C_6H_5O_7{\cdot}2H_2O$ (1.75 mM) was heated to boiling. Then, 0.2 mL $HAuCl_4$ (0.025 M) was added slowly into the above solution. Subsequently, the color of solution turns to wine red. Then, the as-synthesized gold nanoparticle was used for conjugation with BChE and assist DNA S_2. Prior to the experiment, the gold nanoparticle was adjusted to pH ~ 9.0 by Na_2CO_3. Then, 10 μL DNA (S_2, 1 μM) and 60 μL BChE (10 μg mL^{-1}) were injected into the above solution and reacted for 12 h with slightly shaking.

Preparation of aptamer-modified magnetic beads

The aptamer-conjugated magnetic bead was synthesized through strong binding of biotin-streptavidin system. Concretely, the bio-cDNA (10 μL, 1 μM) was injected into the strep-MB (10 μL, 5 mg mL^{-1}) and incubated for 20 min at 37 °C. Following that, the aptamer (20 μL, 1 μM) was added into the mixture and incubated for 1 h. The resultant product was magnetic separation and washed with PBS. Then, the mixture was treated with 0.4 mg mL^{-1} BSA for 1 h to block the space site. Finally, the obtained aptamer-modified magnetic beads (MBs-apt) were dispersed in PBS solution (pH 7.4) for further use.

Competition reaction on magnetic bead and rolling circle amplification

For the detection of malathion, 100 μL of the target with various concentrations was incubated with as-mentioned mixture for 1 h. Concretely, malathion was captured by the aptamer, making the dsDNA unwound to ssDNA. After being washed twice with PBS by magnetic stand, the obtained magnetic beads were dispersed in a mixture that contains ligation buffer (pH 7.8), pDNA (5 μL, 1 μM), and T4 DNA ligase (15 U). The ligation buffer was composed of 10 mM DTT, 40 mM Tris-HCl, 10 mM $MgCl_2$, and 0.5 mM ATP. After reacted for 1 h at 22 °C, the pDNA was linked by T4 DNA ligase to form the circular DNA template. After washing, the precipitates were re-immersed in a reaction buffer (pH 7.9) containing Phi29 DNA polymerase (20 U), dNTPs (5 μL, 10 mM), Phi29 buffer, and BSA (5 μL, 0.4 mg mL^{-1}), with a total volume of 100 μL. The mixture was reacted for 50 min at 37 °C. Then, the as-prepared S_2-Au-BChE signal probe was injected into the mixture and incubated for 1 h. After magnetic separation, the precipitate was reacted with ATCh (50 μL, 10 mM) for 50 min at 37 °C. Thereafter, the supernatant was employed for following PEC measurement.

PEC measurement

Initially, MnO_2 NF@CdS dispersion (20 μL, 20 mg mL^{-1}) was thrown onto the surface of ITO and dried under a stream of air for 30 min. Thereafter, the above supernatant was dropped on the modified electrode and incubated for 40 min. Then, the PEC measurements were performed by the CHI760e electrochemical workstation (CH Instruments, Shanghai, China) equipped with a 500 W xenon lamp as the light source, and the mixture of 0.1 M Na_2S and 0.02 M Na_2SO_3 solution was used as the sacrificial electron donor. The applied potential was 0.01 V. In addition, all determinations were done at least in duplicate.

Results and discussion

Characterization of core-shell MnO_2 NF@CdS nanocomposite

Scheme 1 gives the schematic illustration of photoelectrochemical aptasensing platform for the detection of malathion based on MnO_2 NF@CdS nanocomposite

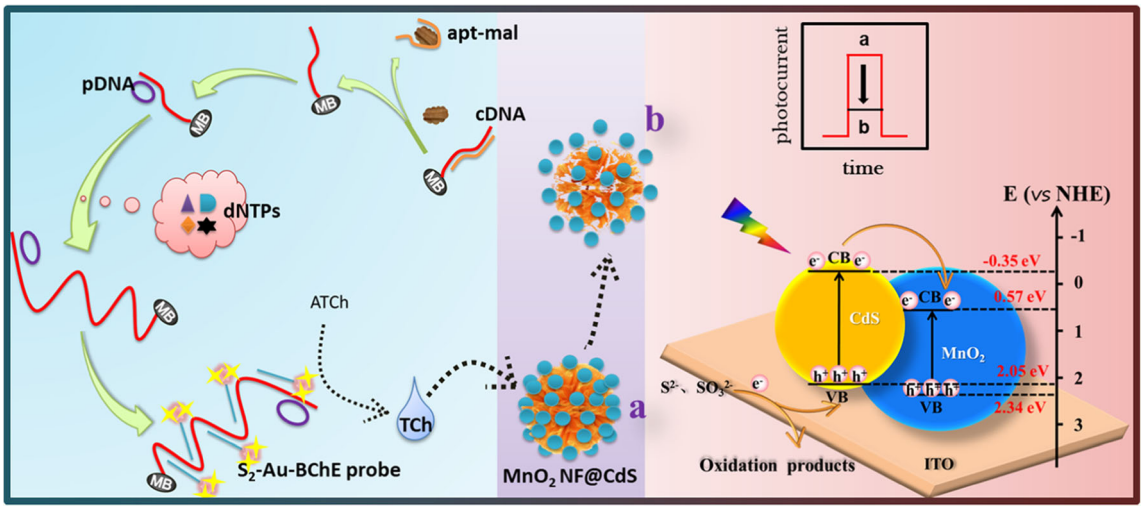

Scheme 1 Schematic illustration of core-shell MnO_2 NF@CdS heterostructure–based signal on photoelectrochemical DNA sensor for determination of malathion by coupling with RCA reaction.

accompanying with RCA. In this system, cDNA combined with MB through the streptavidin-biotin interaction, and hybridized with aptamer. Upon malathion introduction, aptamer was detached from the magnetic beads, while cDNA (with primer fragment) remains on the beads. The primer fragment in cDNA can trigger RCA reaction to form a long single-stranded DNA (ssDNA) strands. Furthermore, a large number of BChE were assembled on the long ssDNA strands through the hybridization with the S_2-Au-BChE probe. Thereafter, TCh, generated from hydrolysis of ATCh by BChE, can reduce MnO_2 NF to Mn^{2+} and release the CdS nanoparticles from the platform electrode. By recording the change in the photocurrent, we could indirectly get the concentration of malathion in the sample. Also, the photoelectric mechanism of MnO_2 NF@CdS composite in PEC detection has been illustrated. Under light irradiation, electron was excited from the occupied valence band (VB) to the empty conduction band (CB) of CdS, while the positive holes were created in the VB of CdS. In this way, the electron-hole pairs were generated. In addition, due to the CB value of CdS was apparently lower than that of MnO_2, the photogenerated electrons would inject into the CB of MnO_2. At the same time, holes on the VB of MnO_2 directly moved to the VB of CdS, and then scavenged by the hole-trapping reagent (Na_2S and Na_2SO_3). Thus, the electron-hole pairs can be effectively separated, resulting in an excellent PEC performance.

To realize our design, the successful synthesis of MnO_2 NF@CdS nanostructures is critically crucial. Scanning electron microscopy (SEM) was applied to characterize the morphology the as-synthesized nanostructures. As shown in Fig. 1A, a complete hierarchical microsphere structure was observed at MnO_2 NF, which was similar to the blooming petals. Unlike the smooth surface of the MnO_2 NF, a rough ball structure can be observed in the images of MnO_2 NF@CdS (Fig. 1B), which seems like that a number of CdS nanoparticles fill into the petals of MnO_2 NF to form core-shell structure. Besides, the size of the nanoparticles was significantly increased. The high-resolution transmission electron microscopy (HRTEM) image of MnO_2 NF@CdS shows that the size of CdS nanoparticles was about 10 nm (Figure S1). Furthermore, the crystalline structure of MnO_2 NF and MnO_2 NF@CdS was investigated by using powder X-ray diffraction. As shown in Fig. 1C, the characteristic diffraction peaks at 12.8°, 25.7°, 36.7°, and 65.1° ascribed to (110), (220), (400), and (002) peaks of MnO_2 with standard tetragonal phase (JCPDS No. 44-0141), indicating the purified tetragonal MnO_2 phase. After CdS NPs was formed on the nanoflower through the hydrothermal method, it is obvious that new diffraction peaks at 24.8°, 26.5°, 28.2°, 36.6°, 43.7°, 52.8°, 54.6°, and 70.9° were acquired, indexing to the (100), (002), (101), (102), (110), (201), (004), and (211) peaks of CdS with a hexagonal structure (JCPDS No. 41-1049) (Fig. 1C, red line), which indicates the successful synthesis of MnO_2 NF@CdS. Noticeably, the sharp peak at 12.8° of MnO_2 was disappeared in red curve due to the stronger peak and better crystallinity of CdS in the nanocomposites. In addition, the energy dispersive spectrometry (EDS) of MnO_2 NF@CdS was displayed in Fig. 1D; all elements including Cd, S, O, and Mn can be found in the nanocomposites. As shown above, it was convinced that the procedure for synthesis of MnO_2 NF@CdS was feasible.

Feasibility investigation of MnO_2 NF@CdS nanocomposite–mediated PEC aptasensing platform

The amplified signal of the developed aptasensing platform comes from the RCA and enzymatic product promoted dissolution of MnO_2 NF@CdS nanocomposites. To realize the design, a puzzling concern arises whether the enzymatic product (TCh) could readily induce the decomposition of MnO_2

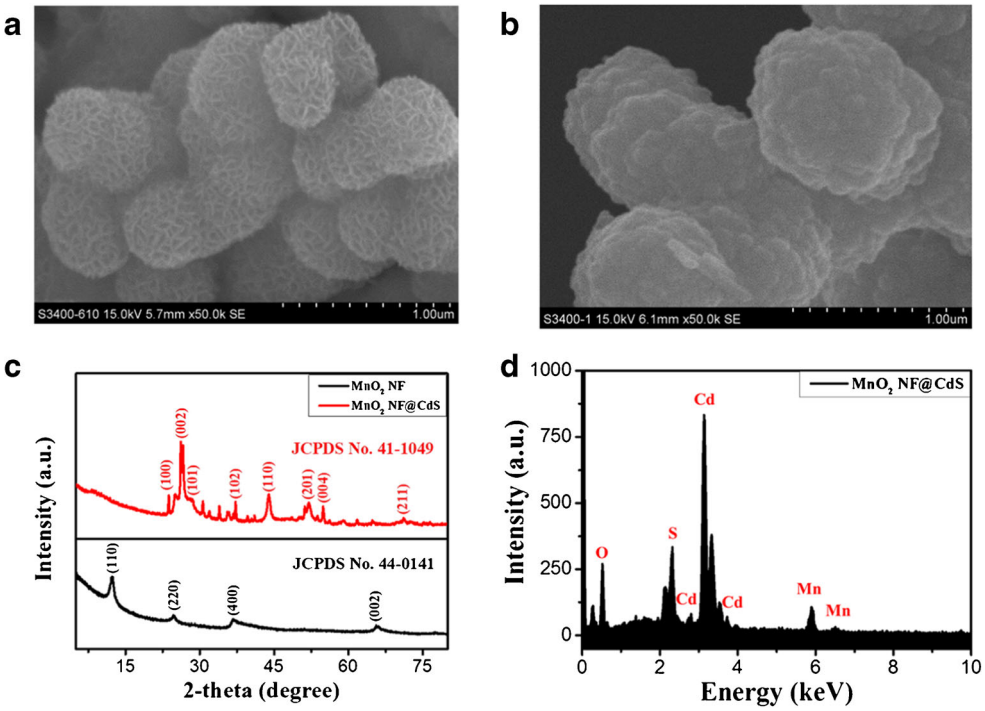

Fig. 1 SEM of (A) MnO_2 NF and (B) MnO_2 NF@CdS; (C) XRD patterns of the MnO_2 NF (blank line) and MnO_2 NF@CdS (red line); (D) EDS of MnO_2 NF@CdS

NF@CdS nanocomposite. To clarify this issue, SEM, UV-visible absorption spectrum, and UV-visible diffuse-reflectance spectrum were employed to characterize the morphology and performance of the MnO_2 NF@CdS nanocomposites before and after treated with TCh. Figure 2A intuitively shows the SEM image of MnO_2 NF@CdS nanocomposite after reacted with TCh. Relative to MnO_2 NF@CdS nanocomposite (Fig. 1B), the surface of the nanocomposite was obviously collapsed and the morphology became irregular. Furthermore, the photocatalytic properties of MnO_2 NF@CdS before (a) and after (b) the dissolution were characterized by photodegradation experiment with methylene blue as substrate (Fig. 2B). It can be clearly seen that the absorbance and the color of methylene blue (MB) obviously decreased and shallowed upon irradiation with visible light due to the photocatalytic decomposition on MnO_2 NF@CdS (curve a). However, the absorbance and color of MB was almost unchanged with the MnO_2 NF@CdS after decomposed by TCh (curve b), implying the decreased photocatalytic ability of nanocomposites. The corresponding photographs exhibit the color of samples. Similar results were also reflected by UV-visible diffuse-reflectance spectrum (DRS). As shown in Fig. 2C, after reacted with TCh, the absorption of MnO_2 NF@CdS nanocomposites in the visible light region from 520 to 700 nm was significantly decreased (curve b). Therefore, TCh can reduce MnO_2 and destroy the MnO_2 NF@CdS heterostructure, thus induce the variations of photoelectrochemical performance.

As mentioned above, for the amplification of the photocurrent signal, a prerequisite lies in the fact that RCA reaction could be readily triggered by the target. Agarose gel electrophoresis was used to monitor the RCA process. As shown in Fig. 2D, lane "b" represents the gel electrophoresis images of RCA product. With a reaction time of 50 min of RCA process, a new bright band appeared at the initial site of this lane "b." It means that the base number was far beyond 2000 bp, which is too long to move forward. The results revealed that the RCA process was successfully performed. Then, the photocurrent characterization of the MnO_2 NF@CdS–based aptasensor with and without target molecule was performed to further testify the feasibility of the designed RCA-amplified strategy. As illustrated in Fig. 2E, curve "b" gives the photocurrent of MnO_2 NF@CdS–modified ITO electrode under the light irradiation, which is significantly higher than that of MnO_2-based ITO electrode (curve "a"), indicating that the co-sensitized structure can promote the charge separation of the nanocomposites and enhance the photocurrent response. Significantly, the photocurrent signal largely decreased in the presence of 60 ng mL^{-1} malathion (curve "c"). The reason might be ascribed that the RCA reaction can be triggered by the target molecule and then a large number of BChE can be assembled on the RCA product. Thus, TCh can be produced from hydrolysis of ATCh by BChE, which can reduce MnO_2 NF to Mn^{2+} and along with releasing CdS nanoparticles from the platform electrode. In contrast, the signal of the strategy was also determined in the absence of malathion (curve "d"), which was almost the same as MnO_2 NF@CdS alone. Actually, when the target was absent, the primer fragment in cDNA was covered by aptamer. Thus, RCA reaction cannot be readily conducted. These results showed that the feasibility of the RCA promoted

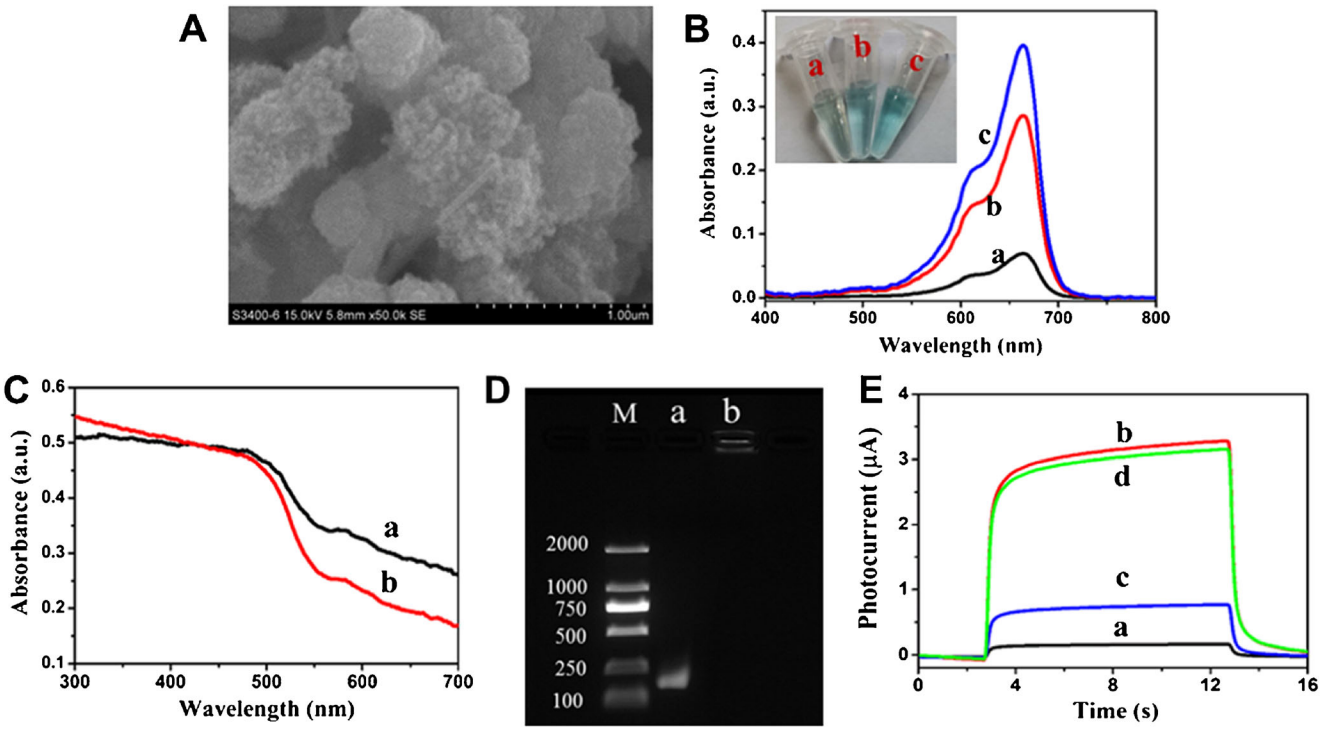

Fig. 2 (A) SEM images of MnO_2 NF@CdS after the decomposition; (B) UV-vis absorption spectra of pristine methylene blue (c) and the mixture of MnO_2 NF@CdS before (a) and after (b) the decomposition (inset: corresponding photographs); (C) UV-visible diffuse-reflectance spectrum of MnO_2 NF@CdS before (a) and after (b) the decomposition; (D) agarose gel electrophoresis image (M: marker, lane a: 1.0 μM cDNA, lane b: the product of RCA); (E) photocurrent responses for (a) MnO_2 NF/ITO, (b) MnO_2 NF@CdS/ITO, and in the presence (c) and absence (d) of 60 ng mL^{-1} target malathion

MnO_2 NF@CdS aptasensor for determination of target malathion.

Optimization of experimental method

Certainly, in order to achieve the optimum detectable signal, several experiment parameters such as RCA reaction time, incubation time between BChE and ATCh, and the decomposition time of MnO_2 NF@CdS were carefully optimized. All the evaluation was based on the photocurrent change ($\Delta I = I_{background} - I_{target}$, where $I_{background}$ and I_{target} were the photocurrent before and after MnO_2 NF@CdS incubated with TCh) by using 60 ng mL^{-1} malathion in this case.

Initially, the effect of RCA reaction time on the photocurrent of this platform was investigated. As seen in Fig. 3A, the change of photocurrent increased with the increasing reaction time and tended to reach a plateau after 50 min. A longer reaction time would not amplify the photocurrent density due to the limitation of the dNTP. To save time with the assay, 50 min was selected as the optimal time of RCA reaction.

In addition, the amount of TCh was highly depended on the incubation time of BChE and decomposition time of MnO_2 NF@CdS. Thus, the incubation time and the decomposition time were investigated. As displayed in Fig. 3B, it is obvious that the signal intensity initially increased with the incubation time of BChE and ATCh, and then tended to be stabilized after 50 min. Hence, 50 min was selected as the optimum incubation time throughout the experiments. Furthermore, in Fig. 3C, with the decomposition time of MnO_2 NF@CdS increasing, more as-modified materials fall from the electrode, resulting in the photocurrent change increased over time and attained the maximum after 40 min. Hence, 40 min was chosen for the whole incubation process.

Moreover, the effect of concentration of ATCh and BChE on the photocurrent of this platform was investigated. From Figure S2, within a certain incubation time, the signal intensity increased with the concentration of ATCh and tended to reach a plateau. So, 10 mM ATCh is suitable for this method. From Figure S3, with the increasing BChE concentration, the signal intensity was obtained to increase to a maximum (at 10 μg/mL). So, 10 μg/mL was chosen for the whole incubation process.

Analytical performance of the core-shell MnO_2 NF@CdS–based PEC platform toward malathion

Under optimal experimental conditions, different concentrations of malathion were measured to verify the ability of the as-proposed PEC aptasensing platform. As illustrated in Fig. 4A, the photocurrent change ($\Delta I = I_{background} - I_{target}$,

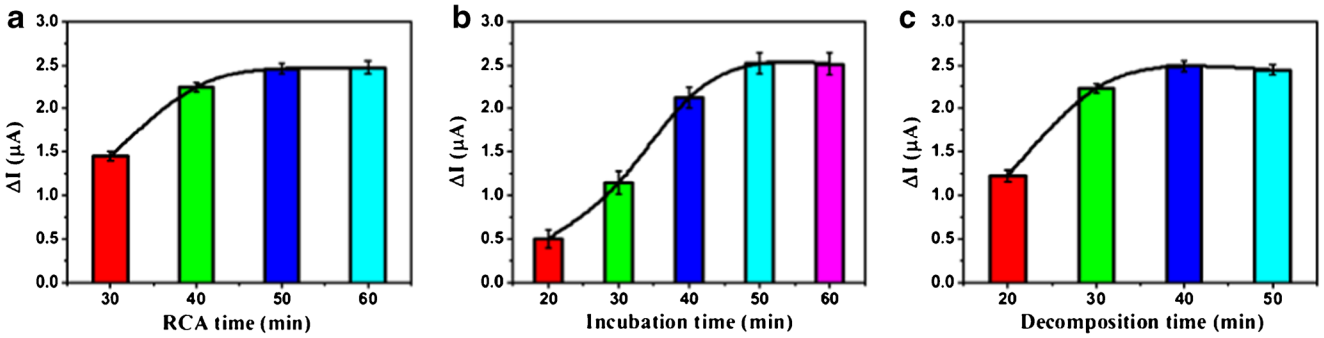

Fig. 3 The effects of (A) reaction time for RCA, (B) incubation time between BChE and ATCh, (C) decomposition time of MnO_2 NF@CdS by TCh. (60 ng mL^{-1} malathion used in this case)

where $I_{background}$ and I_{target} are the photocurrents before and after MnO_2 NF@CdS incubated with TCh) progressively increased with the increment of malathion in the dynamic range of 0.001–100 ng mL^{-1}. Concomitantly, the plot of photocurrent vs the logarithm of insulin concentration showed a linearity with a correlation coefficient of 0.9964 and a linear regression equation of $\Delta I = 1.7266 + 0.4365\ \lg C_{Mal}$ (Fig. 4B). The LOD was calculated as the corresponding amount of the 3-fold background signal generated by the matrix blank and estimated to be approximately 0.68 pg mL^{-1}. In addition, the linear range and detection limit of this method was comparable with other reports (Table S1).

The selectivity and specificity of the PEC aptasensor was evaluated toward some nontarget analytes with the results illustrated in Fig. 4C, e.g., dichlorvos (Dic) and chlorpyrifos (Chl). In this case, the aptasensing platform did not respond to both Dic and Chl at higher concentrations and negligible response was obtained in the nontarget solution, indicating few nonspecific binding. Inversely, the photocurrent signal in the mixture of target malathion with nontargets is similar to malathion alone, which revealed the acceptable specificity of the detection system. Similarly, the stability and reproducibility of MnO_2 NF@CdS–based PEC aptasensor were also crucial for the development of a new analytical method. Corresponding to the 60 ng mL^{-1} malathion, Fig. 4D displays the operational stability of the sensor, which were recorded in the absence (a) and presence (b) of target with 10 repeated switching on and off the lamp, revealing an

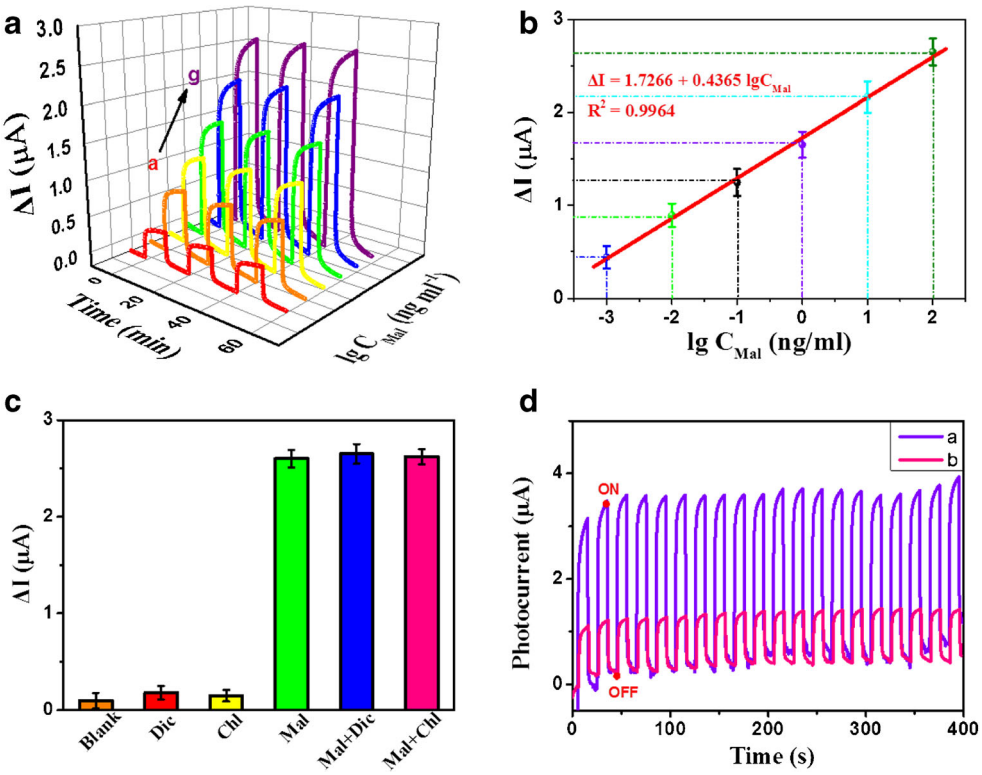

Fig. 4 (A) Photocurrent responses of RCA signal amplified PEC biosensor to different target malathion with various concentrations (a–g: 0.001, 0.01, 0.1, 1, 10, 100 ng mL^{-1}); (B) the corresponding calibration curve; (C) the specificity of the PEC DNA biosensor (malathion: 100 ng mL^{-1}, interfering substance: 2 mg mL^{-1}); (D) stability evaluation in the absence (a) or presence (b) of malathion

Table 1 Determination of the malathion in red wine and milk with the proposed PEC DNA sensor

	Sample	Added (ng mL^{-1})	RSD (%)	Recovery (%)
Red wine	1	0.001	2.5	100.4
	2	0.1	4.0	99.9
	3	0.5	3.4	100.1
	4	1	3.7	98.2
	5	10	3.5	97.8
Milk	1	0.001	2.8	98.8
	2	0.1	4.9	100.3
	3	0.5	3.4	99.5
	4	1	4.6	99.1
	5	10	2.4	100.1

excellent stability of the electrode. Then, the reproducibility was investigated by repeating the test five times, and the relative standard deviation (RSD) value of 8.9% indicated a benign reproducibility.

Recovery measurement

To study the reliability of the newly developed detection system in foodstuff, one precondition should meet the needs of recovery in the complex system such as diluted milk and red wine with the target concentrations of 0.001, 0.01, 0.5, 1, 10 ng mL^{-1}, respectively. For milk, the recoveries shift from 98.8% to 100.3% and the relative standard deviation transform from 2.4% to 4.9%. And for red wine, the recoveries of the aptasensor range from 97.8 to 100.4% and the RSD varies from 2.5 to 4.0% (Table 1).

In addition, the apple juice sample containing different malathion was monitored by the developed PEC biosensor and a referenced gas chromatography method, respectively. As shown in Fig. 5, a well-positive correlation was displayed in the regression equation between two methods with a slope of 1.1089 ± 0.06, an intercept of -2.4548 ± 1.55, and a correlation coefficient of 0.9899. The results demonstrated a favorable accuracy of the proposed method in the complex samples.

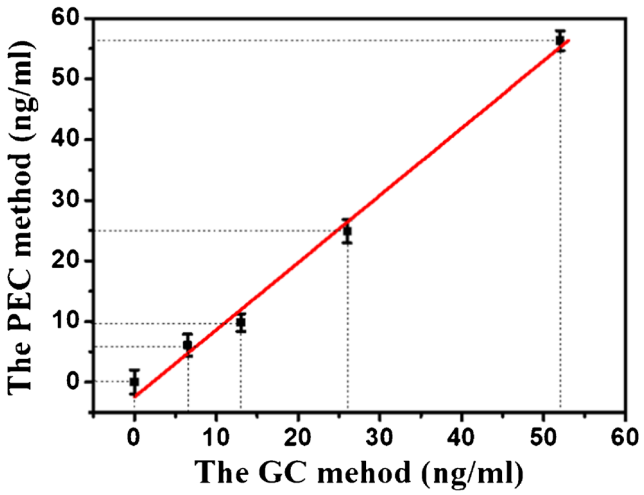

Fig. 5 Comparison of the results for malathion in apple juice obtained by using this PEC assay and the referenced gas chromatography, respectively ($n = 3$)

Conclusions

In summary, this work constructed a novel split-type photoelectrochemical aptasensing platform based on MnO_2 NF@CdS nanocomposite for the sensitive detection of organophosphorus pesticide (malathion acted as the model analyte). The MnO_2 nanoflower with a complete hierarchical microsphere structure provided high surface area for loading multiple CdS nanoparticles. Under solar irradiation, the nanocomposites present excellent photocurrent response. Experiment shows that the photocatalytic performance of the nanostructure was highly lowed after it treated with TCh, which might be ascribed to decomposition of the MnO_2 NF@CdS nanocomposites. By recording the change in the photocurrent, we could indirectly get the concentration of malathion in the sample. Furthermore, the signal amplification of the aptasensor was dependent on target-triggered RCA reaction. The high loading of RCA product can assemble multiple BChE, which can convert ATCh to TCh, decomposing MnO_2 NF@CdS nanocomposite–based photoactive material. Thus, remarkable signal changes are generated. As expected, experimental results showed that our protocol displayed a wide linear range with high sensitivity and good reproducibility in determination of malathion, even in a complex environment. Accordingly, this strategy may have extensive use in other targets by changing the design of the binding aptamer.

Funding information This work was financially supported by the National Natural Science Foundation of China (21864013; 21802133), the Open Project Program of Key Laboratory of Functional Small Organic Molecule, Ministry of Education, Jiangxi Normal University (No. KLFS-KF-201917), and China outstanding Youth Funds of Jiangxi Normal University.

Compliance with ethical standards

Conflict of interest The authors declare that they have no competing interests.

References

1. Yan X, Song Y, Zhu C, Li H, Du D, Su X, Lin Y (2018) MnO_2 nanosheet-carbon dots sensing platform for sensitive detection of organophosphorus pesticides. Anal Chem 90:2618–2624
2. Lv B, Wei M, Liu Y, Liu X, Wei W, Liu S (2016) Ultrasensitive photometric and visual determination of organophosphorus

pesticides based on the inhibition of enzyme-triggered formation of core-shell gold-silver nanoparticles. Microchim Acta 183:2941–2948
3. Gai P, Zhang S, Yu W, Li H, Li F (2018) Light-driven self-powered biosensor for ultrasensitive organophosphate pesticide detection via integration of the conjugated polymer-sensitized CdS and enzyme inhibition strategy. J Mater Chem B 6:6842–6847
4. Zhao Y, Yang M, Fu Q, Ouyang H, Wen W, Song Y, Zhu C, Lin Y, Du D (2018) A nanozyme- and ambient light-based smartphone platform for simultaneous detection of dual biomarkers from exposure to organophosphorus pesticides. Anal Chem 90:7391–7398
5. Cacho JI, Campillo N, Viñas P, Hernández-Córdoba M (2018) In situ ionic liquid dispersive liquid-liquid microextraction coupled to gas chromatography-mass spectrometry for the determination of organophosphorus pesticides. J Chromatogr A 1559:95–101
6. Su R, Li D, Wang X, Yang H, Shi X, Liu S (2016) Determination of organophosphorus pesticides in ginseng by carbon nanotube envelope-based solvent extraction combined with ultrahigh-performance liquid chromatography mass spectrometry. J Chromatogr B 1022:141–152
7. Cequier E, Sakhi AK, Haug LS, Thomsen C (2016) Development of an ion-pair liquid chromatography–high resolution mass spectrometry method for determination of organophosphate pesticide metabolites in large-scale biomonitoring studies. J Chromatogr A 1454:32–41
8. Zhang L, Shen Y, Fan G, Xiong M, Yu X, Zhao W (2019) Preparation of an AgI/$CuBi_2O_4$ heterojunction on a fluorine-doped tin oxide electrode for cathodic photoelectrochemical assays: application to the detection of L-cysteine. Microchim Acta 186: 284–291
9. Li X, Kong W, Qin X, Qu F, Lu L (2020) Self-powered cathodic photoelectrochemical aptasensor based on in situ-synthesized CuO-Cu_2O nanowire array for detecting prostate-specific antigen. Microchim Acta 187:325–333
10. Shu J, Tang D (2020) Recent advances in photoelectrochemical sensing: from engineered photoactive materials to sensing devices and detection modes. Anal Chem 92:363–377
11. Tang J, Xiong P, Li J, Cheng Y, Tian X, Chen Y, Sun Y, Tang D (2019) Target-induced elimination of photosensitizer and formation insulation layer enabling ultrasensitive photoelectrochemical detection of ochratoxin A. Sens Actuators B Chem 297:126707
12. Deng H, Huang L, Chai Y, Yuan R, Yuan Y (2019) Ultrasensitive photoelectrochemical detection of multiple metal ions based on wavelength-resolved dual-signal output triggered by click reaction. Anal Chem 91:2861–2868
13. Tang J, Xiong P, Cheng Y, Chen Y, Peng S, Zhu Z (2019) Enzymatic oxydate-triggered AgNPs etching: a novel signal-on photoelectrochemical immunosensing platform based on Ag@AgCl nanocubes loaded RGO plasmonic heterostructure. Biosens Bioelectron 130:125–131
14. Ge L, Hong Q, Li H, Liu C, Li F (2019) Direct-laser-writing of metal sulfide-graphene nanocomposite photoelectrode toward sensitive photoelectrochemical sensing. Adv Funct Mater 29:1904000
15. Luo J, Liang D, Li X, Deng L, Wang Z, Yang M (2020) Aptamer-based photoelectrochemical assay for the determination of MCF-7. Microchim Acta 187:257–263
16. Jia J, Wu J, Dong J, Fan L, Huang M, Lin J, Lan Z (2018) Cadmium sulfide as an efficient electron transport material for inverted planar perovskite solar cells. Chem Commun 54:3170–3173
17. Zhang X, Zhang R, Yang A, Wang Q, Kong R, Qu F (2017) Aptamer based photoelectrochemical determination of tetracycline using a spindle-like ZnO-CdS@Au nanocomposite. Microchim Acta 184:4367–4374
18. Vaquero F, Navarro RM, Fierro JLG (2017) Influence of the solvent on the structure, morphology and performance for H_2 evolution of CdS photocatalysts prepared by solvothermal method. Appl Catal B 203:753–767
19. Zhang J, Li W, Li Y, Zhong L, Xu C (2017) Self-optimizing bifunctional CdS/Cu_2S with coexistence of light-reduced Cu^0 for highly efficient photocatalytic H_2 generation under visible-light irradiation. Appl Catal B 217:30–36
20. Yang H, Lu M, Chen D, Chen R, Li HW (2019) Efficient and rapid removal of Pb^{2+} from water by magnetic Fe_3O_4@MnO_2 core-shell nanoflower attached to carbon microtube: adsorption behavior and process study. J Colloid Interface Sci 563:218–228
21. Ma Q, Wang H, Zhang H, Cheng X, Xie M, Cheng Q (2017) Fabrication of MnO_2/TiO_2 nano-tube arrays photoelectrode and its enhanced visible light photoelectrocatalytic performance and mechanism. Sep Purif Technol 189:193–203
22. Mo Z, Xu H, Chen Z, She X, Song Y, Lian J, Zhu X, Yan P, Lei Y, Yuan S, Li H (2019) Construction of MnO_2/monolayer g-C_3N_4 with Mn vacancies for Z-scheme overall water splitting. Appl Catal B 241:452–460
23. Rahmat M, Rehman A, Rahmat S, Bhatti HN, Iqbal M, Khan WS, Bajwa SZ, Rahmat R, Nazir A (2019) Highly efficient removal of crystal violet dye from water by MnO_2 based nanofibrous mesh/photocatalytic process. J Mater Res Technol 8:5149–5159
24. Lin Y, Zhou Q, Tang D, Niessner R, Knopp D (2017) Signal-on photoelectrochemical immunoassay for aflatoxin B1 based on enzymatic product-etching MnO_2 nanosheets for dissociation of carbon dots. Anal Chem 89:5637–5645
25. Zhang X, Zhao C, Shu Y, Wang J (2019) Gold nanoclusters/iron oxyhydroxide platform for ultrasensitive detection of butyrylcholinesterase. Anal Chem 91:15866–15872
26. Zhang K, Lv S, Lin Z, Li M, Tang D (2018) Bio-bar-code-based photoelectrochemical immunoassay for sensitive detection of prostate-specific antigen using rolling circle amplification and enzymatic biocatalytic precipitation. Biosens Bioelectron 101:159–166
27. Li M, Xu X, Cai Q, Luo X, Zhou Z, Xu G, Xie Y (2019) Graphene oxide-based fluorometric determination of microRNA-141 using rolling circle amplification and exonuclease III-aided recycling amplification. Microchim Acta 186:531–537
28. Hu J, Zhang C (2010) Sensitive detection of nucleic acids with rolling circle amplification and surface-enhanced raman scattering spectroscopy. Anal Chem 82:8991–8997
29. Cheng X, Yu X, Chen L, Zhang H, Wu Y, Fu F (2017) Visual detection of ultra-trace levels of uranyl ions using magnetic bead-based DNAzyme recognition in combination with rolling circle amplification. Microchim Acta 184:4259–4267
30. Aveiro LR, da Silva AGM, Antonin VS, Candido EG, Parreira LS, Geonmonond RS, de Freitas IC, Lanza MRV, Camargo PHC, Santos MC (2018) Carbon-supported MnO_2 nanoflowers: introducing oxygen vacancies for optimized volcano-type electrocatalytic activities towards H_2O_2 generation. Electrochim Acta 268:101–110
31. Ibrahim I, Lim HN, Abou-Zied OK, Huang NM, Estrela P, Pandikumar A (2016) Cadmium sulfide nanoparticles decorated with au quantum dots as ultrasensitive photoelectrochemical sensor for selective detection of copper (II) ions. J Phys Chem C 120: 22202–22214